CHAPTER II
LITERATURE REVIEWS

This chapter will primarily introduce the knowledge related to $BiFeO_3$ (BFO) thin films, including their structure, production, and properties. It will also review the nanopatterning method and its effects on BFO Thin film. There are two main mechanisms that explain the effect of light irradiation on the surface of the sample. Firstly, dynamic mechanism includes the photoelectric photoconductivity, and ferroelectric photovoltaic effects. While two-dimensional electron gases and oxygen vacancy are categorized as a non-dynamic mechanism.

2.1 Bismuth Ferrite ($BiFeO_3$)

The study of BFO was initiated by Smolenskii in 1959, revealing its potential as a multiferroic material. However, due to the difficulty in growing single-phase BFO, it did not attract much interest from researchers at the time (Smolenskii, 1959). By the late 1960s, researchers proposed a solution to this problem by treating BFO with HNO_3 (nitric acid) to eliminate secondary phases. This approach successfully synthesized single-phase BFO (Achenbach et al., 2006; Michel et al., 1969). A significant milestone occurred a few decades later when Kubel and Schmid discovered the monodomain single-phase BFO in 1990 using X-ray diffraction measurement, which revealed its intrinsic properties (Kubel et al., 1990). In 2003, Another milestone was set when Wang et al. demonstrated a significant ferroelectric polarization of approximately 60 $\mu C/cm^2$ in BFO epitaxial thin films grown on an SRO/STO substrate, which is about 15 times higher than that of bulk BFO (Wang et al., 2003). This marked the first instance of achieving such high polarization in BFO thin films, opening new opportunities for use in memory devices and next-generation spintronic devices.

At room temperature, the single-phase structure of BFO is described as a rhombohedral distorted perovskite, categorized under the R3c space group (Moreau et al., 1971). Figure 2.1 shows the structure of perovskite BFO, where the Bi ion is located at the corners, the Fe ion at the center, and 6 oxygen ions at the face centers (Hiroshi, 2011). BFO exhibits ferroelectric properties below its Curie temperature ($T_C \approx 1103$ K) and antiferromagnetic properties below its Néel temperature ($T_N \approx 643$ K) in ceramic bulk form (Sosnowska et al., 1982). The rhombohedral structure of perovskite BFO has lattice parameters of a = 3.96 Å and a rhombohedral angle of α = 89.4° at room temperature. It exhibits ferroelectric polarization along the pseudocubic [111] direction .

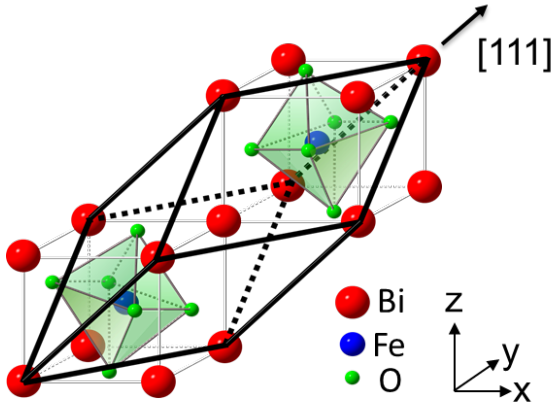

Figure 2.1 A diagram showing the rhombohedral structure of perovskite BFO, which belongs to the R3c space group, with two unit cells aligned along the [111] direction. (Hiroshi, 2011).

2.1.1 Bismuth ferrite thin films preparation

BFO thin films can be prepared using various thin film deposition methods. These methods include metal organic chemical vapor deposition (MOCVD), electron beam (e-beam) evaporation, pulsed-laser deposition (PLD), spray pyrolysis, chemical solution deposition (CSD), the sol-gel method, and radio frequency (RF) magnetron sputtering. Each method has its own set of trade-offs between cost, complexity, film quality, and suitability for different applications. Hence, the choice of method depends on the specific requirements of the BFO thin films. For instance, MOCVD and spray pyrolysis are generally employed to grow films at high temperatures, around 800 °C (Micard et al., 2020). As a result, these techniques are unsuitable for

producing BFO thin films intended for low operating temperatures. While PLD and e-beam evaporation are limited to growing films on small substrate areas. Consequently, these techniques are unsuitable for producing large-scale homogeneous thin films (Mijiti et al., 2021; Pei et al., 2020; You et al., 2018; Zhang et al., 2018). CSD and sol-gel methods apply thin films to substrates at ambient temperature. However, these films require high post-annealing temperatures, around 700 °C, for crystallization (Yang et al., 2021). As a result, RF magnetron sputtering is often chosen for growing high-quality thin films on large area substrates at low temperatures. This method is straightforward, easy to scale up, and highly compatible with electronic industry needs (Li et al., 2008; Wu et al., 2010; Zhu et al., 2018).

The RF magnetron sputtering method uses alternating current (AC) to avoid charge buildup on the oxide sputtering target. The process begins by evacuating the sputtering chamber to reach a high vacuum level of 10^{-7} Torr. Next, an inert gas like argon is introduced into the chamber, increasing the pressure to 10^{-3} Torr. A RF voltage is applied between the substrate (anode) and the target (cathode). As the power supply gradually increased, the argon gas ionizes into Ar^{+} ions and electrons. The Ar^{+} ions gain energy corresponding to the voltage between the substrate and the target, accelerating due to the electric field from the applied voltage and bombarding the target surface. Atoms are sputtered off the target, becoming vapor and then depositing on the substrate. Meanwhile, the ionized electrons are trapped near the target by magnets placed behind the cathode, enhancing the bombardment process. (Feng, 2018). Figure 2.2 illustrates a schematic diagram of the fundamental components of a magnetron sputtering system.

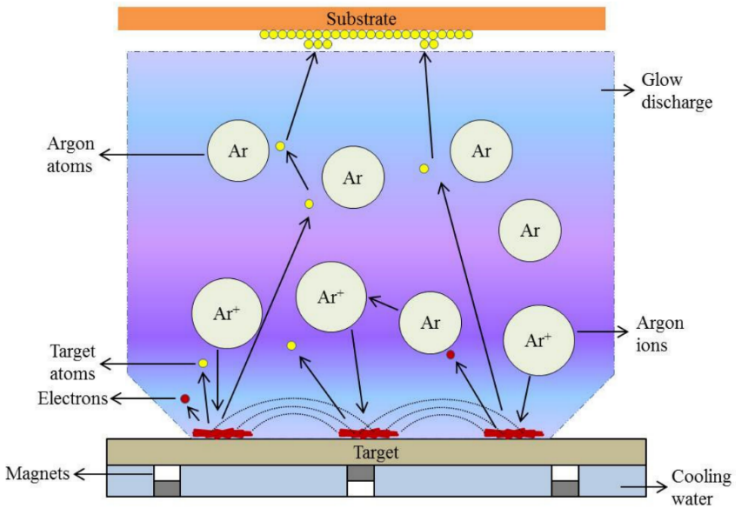

Figure 2.2 The schematic diagram of the fundamental components of a magnetron sputtering system (Maurya et al., 2014).

2.1.2 Ferroelectric property in Bismuth ferrite thin films

Ferroelectric materials exhibit spontaneous electric polarization, which can be switched by applying an electric field (Lines et al., 2001). In perovskite oxide materials, the ferroelectric phase occurs when they transition from a centrosymmetric cubic phase at high temperatures to a lower symmetry phase below the transition temperature, known as the Curie temperature. This mechanism occurs when cations move relative to the anions in the oxide perovskite, creating an electric dipole moment that results in spontaneous polarization. At room temperature, ceramic bulk BFO exhibits both ferroelectric and antiferromagnetic properties because of its high Curie temperature ($T_C \approx 1103$ K) and Néel temperature ($T_N \approx 643$ K) (Sosnowska et al., 1982). In 2003, researchers observed a significant remanent polarization of around 60 μC/cm² in 200-nm-thick epitaxial BFO thin films grown on an SRO/STO (001) substrate for the first time, as depicted in Figure 2.3(a) (Wang et al., 2003). These thin films showed a spontaneous polarization at room temperature that was higher than the bulk BFO, which is approximately 6.1 μC/cm² (Teague et al., 1970).

Approximately a year later, researchers investigated how substrate orientation affects ferroelectric properties. They grew pure phase of BFO thin films with thickness 200 nm on (111), (101), and (001) SRO/STO substrates. The hysteresis loops for these orientations showed remanent polarization (P_r) values of around 100, 80, and 55 μC/cm² for (111), (101), and (001) STO substrates, respectively. A single crystal with a rhombohedral structure of BFO films grown on the (111) orientation was exhibited, while those on the (101) or (001) orientations were monoclinically distorted from the rhombohedral structure due to the epitaxial constraint (Li et al., 2004). Similarly, Das et al. also prepared 600-nm-thick BFO thin films on STO substrates with (001), (101), and (111) orientations. The resulting hysteresis loops showed remanent polarization (Pr) values of approximately 98, 86, and 55 μC/cm² for (111), (101), and (001) STO substrates, respectively, as illustrated in Figure 2.3(b) (Das et al., 2006). Both studies suggest that the direction of spontaneous polarization is nearly aligned with the (111) orientation, similar to that observed in bulk crystals and ceramics.

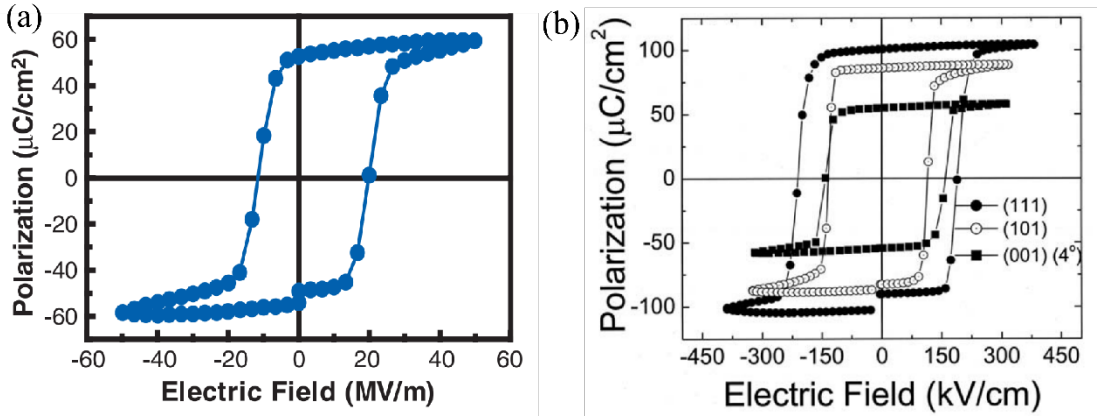

Figure 2.3 The hysteresis loop of BFO/SRO/STO sample (a) at 15 kHz (Wang et al., 2003) and (b) at orientation of (111), (101), and (001) BFO films (Das et al., 2006).

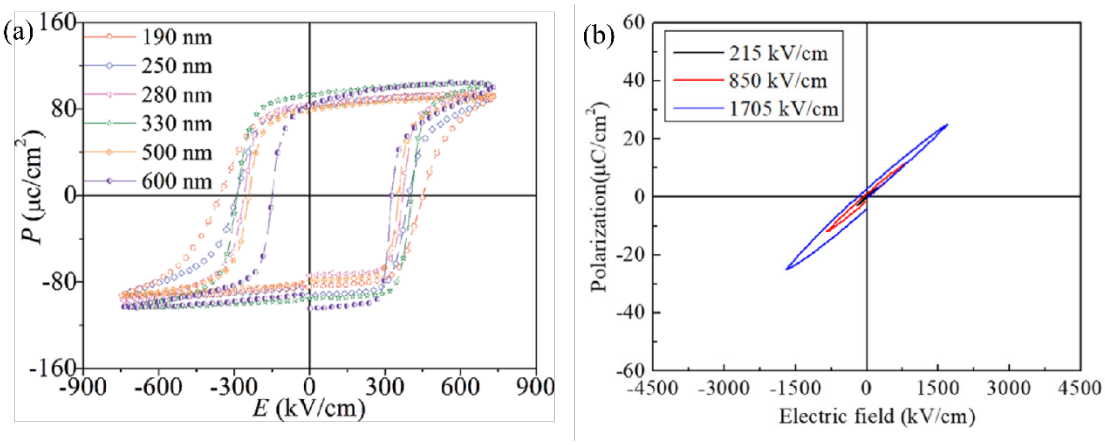

Figure 2.4 The hysteresis loop (a) BFO thin films different thicknesses of 190-600 nm on SRO/Pt/TiO_2/SiO_2/Si substrate at 1 kHz (Wu et al., 2011) and (b) various electric fields of amorphous BFO thin films on Pt/Ti/SiO_2/Si substrate (Li et al., 2021).

Pure phase BFO thin films with varying thicknesses from 190 to 600 nm were grown on SRO/Pt/TiO_2/SiO_2/Si (100) substrates using RF sputtering. At 1 kHz and room temperature, these films exhibited significant polarization, ranging from about 80 to 95 μC/cm², with a mixture of (110) and (111) orientations, as shown in Figure 2.4(a) (Wu et al., 2011). The highest spontaneous polarization is observed in the (111) direction for BFO thin films because ions are displaced along the pseudocubic [111] direction from their equilibrium positions (Ederer et al., 2005). Consequently, the combination of both orientations greatly improves the ferroelectric properties of BFO thin films.

2.1.3 Nanolithography on Bismuth ferrite thin films

Nanolithography techniques have emerged as vital tools in this field, enabling the creation of nanostructures with precise control over their size and properties. Among these techniques, Dip-Pen Nanolithography (DPN), Electron Beam Lithography (EBL), and Focused Ion Beam (FIB) milling have been extensively explored for fabricating BFO nanostructures. Each method offers unique advantages and limitations, which can significantly impact their suitability for specific applications.

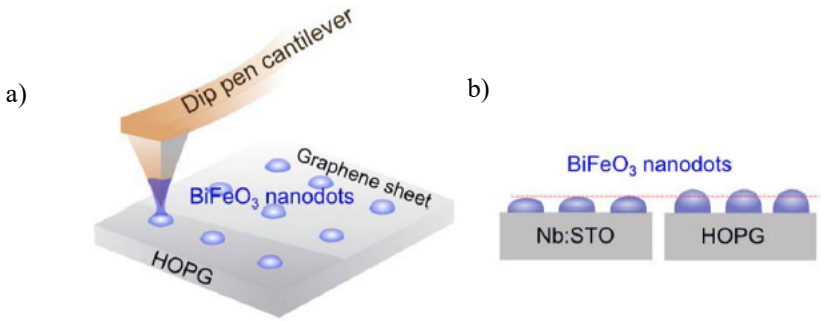

Figure 2.5 Schematic diagrams showing the DPN of BFO nanodots: (a) a nano-pattern using a BFO precursor sol by DPN, (b) BFO nanodots prepared on Nb-STO and HOPG substrates (Kim et al., 2013).

Dip-Pen Nanolithography (DPN) uses an atomic force microscope (AFM) tip to precisely deposit materials onto a surface. The AFM tip, typically made of silicon, is dipped into an "ink" solution containing the material to be deposited. When the tip touches the surface, a small liquid bridge forms, allowing the material to transfer and create patterns. The movement of the AFM tip is carefully controlled, allowing for the creation of very small and precise structures. After the material is deposited, the surface is often heated to improve its properties. DPN can use various materials and is useful for making tiny electronic components and sensors. This method doesn't require additional steps like masks, making it a simple and effective way to create nanoscale patterns (Jung et al., 2012).

EBL is a high-resolution nano-patterning method that employs a focused beam of electrons to produce accurate patterns on a substrate (Tseng et al., 2003). The process begins with coating the substrate with an electron-sensitive resist, typically a polymer like polymethyl methacrylate (PMMA) (Shahali et al., 2019). The substrate is then exposed to a focused electron beam that scans the surface according to a computer-aided design (CAD) file. This exposure changes the chemical structure of the resist in the scanned areas. The substrate is then developed, dissolving the exposed areas of the resist in positive resists or the unexposed areas in negative resists. The remaining resist pattern acts as a mask for subsequent etching or material

deposition steps. Finally, the remaining resist is then removed, leaving the desired pattern on the substrate (Chen, 2015).

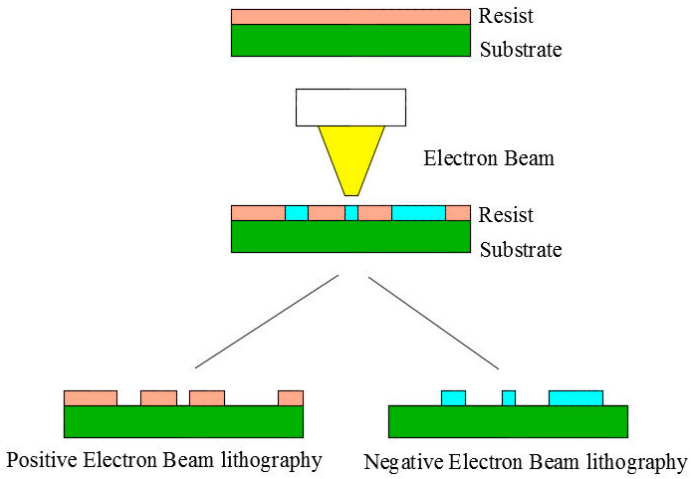

Figure 2.6 The Principal of EBL (Shahali et al., 2019).

FIB milling is a high-resolution fabrication technique (10-30 nm) used for imaging and fabricating various materials, such as silicon wafers, polymers, and metals. The FIB principle is similar to that of Scanning Electron Microscopy (SEM), but instead of electrons, it uses ions like Ga^+, Ne^+, or He^+ (Rodriguez Hernandez et al., 2015). As shown in Figure 2.7, the interaction volumes of gallium ions, electrons, and helium ions differ. The interaction volume for secondary electrons (SE) produced by a focused He+ beam is much smaller than that produced by electrons or Ga^+, meaning that a Helium Ion Microscope (HIM) provides better resolution for imaging compared to Ga^+-FIB and SEM. Conversely, Ga^+ ions have a high mass, causing significant surface scattering. HIM can also scatter the surface at 30 keV, and because He^+ ions have a low mass, it is advantageous for fabricating very small features at the sub-nanometer scale (Hlawacek et al., 2014).

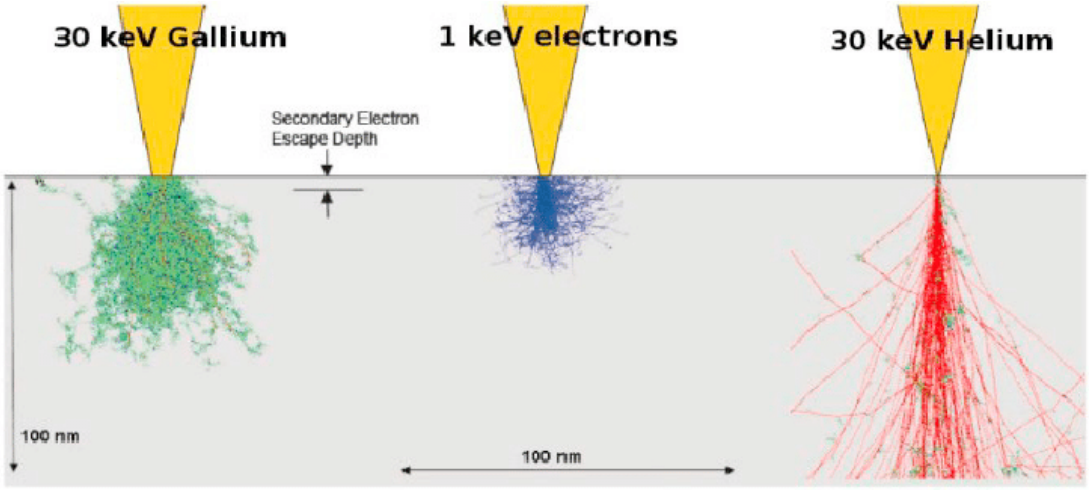

Figure 2.7 Differences in interaction volumes among various charged particle beams used for imaging (Hlawacek et al., 2014).

In 2006, Tao Sun and colleagues reported the fabrication of BFO nanopatterns using soft electron beam lithography, which combines electron beam lithography with the spinning of sol-gel precursors on an STO substrate (Sun et al., 2006). Firstly, a polymer and PMMA were sequentially spun onto the substrates as electron beam resist. The electron beam was then used to pattern arrays of disks or lines on the resist. BFO sol was spun onto the substrate and dried at 150°C to gel the sol after developing. The samples were then immersed in acetone to remove the electron beam resist and remove excess BFO from the unpatterned areas. Finally, crystalline BFO patterns were obtained by annealing the samples at 600°C for 30 minutes. The BFO nanolines with 80 nm of linewidth patterned on STO substrate exhibit an bamboolike microstructure that could be useful for studying the role of grain boundaries in influencing the leakage current in BFO (Sun et al., 2006).

In 2012, Inhwa Jung and colleagues used Dip-Pen Nanolithography (DPN) with a silicon nitride cantilever to create BFO nanodots on a NSTO substrate. The size of the BFO nanodots ranged from 30 to 180 nm, depending on the deposition time, which varied between 0.1 and 10 seconds. The array of BFO nanodots was well-formed, with a minimum gap of around 30 nm between the dots (Jung et al., 2012). Notably, the minimum-sized BFO nanodot is characterized to be a single domain with the lateral dimension of 30 nm and thickness of 16 nm. It also showed a good

ferroelectric switching characteristics with only 1V bias potential. One year later, Woo-Hee-kim and colleagues investigated the comparative BFO nanodot study between NSTO and highly ordered pyrolytic graphite (HOPG) substates using Dip-Pen Nanolithography (DPN). The result suggested that BFO nanodot on the HOPG substrate is smaller in lateral size and higher in thickness compared to NSTO substrate. Additionally, PFM measurements showed that BFO nanodots on HOPG have better ferroelectric properties compared to those on NSTO, with a ratio of 1.2:1. This is due to the reduced substrate clamping effect and improved piezoresponse properties (Kim et al., 2013).

In 2009, Seungbum Hong and co-workers fabricated epitaxial BFO nanostructures with three layers BFO, SRO and STO respectively from top to bottom. The BFO layer was patterned into the square shape of 500x500 nm^2 in size and round shape of 500 nm in diameter by using focused Ion beam (FIB) lithography. They reported the ferroelectric domain configuration and switching behavior depend on the shapes. Square-shaped nanostructures show a single variant domain, whereas round-shaped nanostructures display seven variants of domain configuration. They also found that the round-shaped nanostructures provide more symmetric hysteresis loops (Hong et al., 2009). In 2018, Bumsoo Kim and colleagues used angle-resolved piezorespose force microscope (AR-PFM) to investigated ferroelectric domain in BFO/SRO/STO substrate patterned by combined EBL and FIB techniques. They found that the removal of the film surrounding the structures from patterning caused elastic relaxation, leading to a reduction in the average number of neighboring domains. This indicates a decrease in domain complexity. Additionally, the result also revealed that the higher aspect ratio patterning structures provides a simpler domain configuration and better piezoresponse characteristics, such as lower coercive voltage and higher remanent piezoresponse (Kim et al., 2018) as illustrated in Figure 2.8.

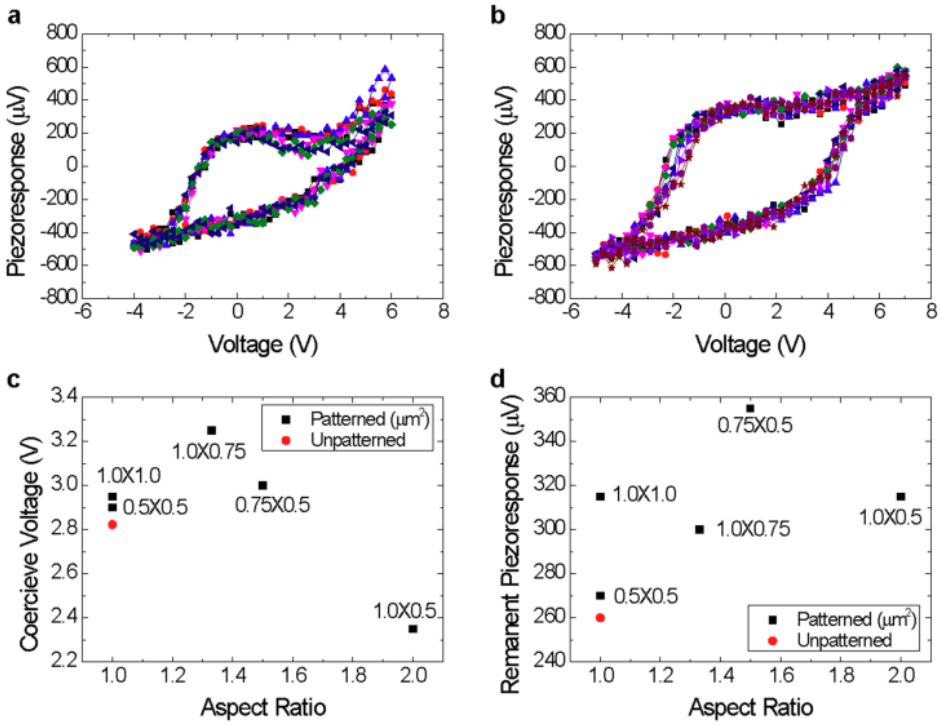

Figure 2.8 Piezoresponse measurement for (a) unpatterned BFO film and (b) 0.75 μm×0.5 μm patterned BFO structure. (c) Coercive voltage and (d) remanent piezoresponse of the patterned BFO structures and the unpatterned BFO film (Kim et al., 2018).

2.2 Dynamic mechanism

2.2.1 Photoelectric effect

The photoelectric effect is a phenomenon in which electrons are emitted from a material's surface upon absorbing electromagnetic radiation, a process also known as photoemission. The emitted electrons are termed photoelectrons. Discovered by Heinrich Hertz in 1887, the photoelectric effect was observed when ultraviolet light shone on two metal electrodes with a voltage applied across them, causing a change in the voltage between the electrodes. This phenomenon, which classical physics could not explain, demonstrated the interaction between light and matter and characterized light as an electromagnetic wave. In 1905, Einstein explained through quantum mechanics that each particle of light, called a photon, carries a fixed amount of energy, given by ($\mathrm{E} = \mathrm{h}\nu$), where ν is the light's frequency and h is Planck's

constant. The work function (w) is a metal's intrinsic property, representing the minimum energy required to remove an electron from the metal's surface. When the energy of a photon exceeds the work function, the kinetic energy ($\mathrm{E_k}$) of the ejected electron can be expressed as shown in equation (2.1).

$$\mathrm{E_k} = \mathrm{h\nu} - \mathrm{w} \tag{2.1}$$

Where $\mathrm{E_k}$ is the kinetic energy of the ejected electron, h**ν** is the energy of the incident photon. When an electron is ejected, the incident photon's energy (h**ν**) must overcome both the binding energy ($\mathrm{E_b}$) and work function (w). Therefore, we can write in (2.2).

$$\mathrm{h\nu} = \mathrm{E_b} + \mathrm{w} + \mathrm{E_k} \tag{2.2}$$

The kinetic energy of the ejected electron can be written as in equation (2.3).

$$\mathrm{E_k} = \mathrm{h\nu} - \mathrm{E_b} - \mathrm{w} \tag{2.3}$$

From this equation, the binding energy can be represented as shown in equation (2.4).

$$\mathrm{E_b} = \mathrm{h\nu} - \mathrm{E_k} - \mathrm{w} \tag{2.4}$$

2.2.2 Ferroelectric photovoltaic effect

Ferroelectric materials have the ability to exhibit spontaneous polarization, which can be switched by applying an external electric field (Lines et al., 2001). When light interacts with ferroelectric materials, it generates pairs of electrons and holes, leading to a steady-state photocurrent, a phenomenon known as the photovoltaic effect. Ferroelectric photovoltaic (FEPV) effects occur in these materials, producing photovoltage and photocurrent along the polarization direction. FEPV effects differ from conventional photovoltaic devices in two key aspects. Firstly, in typical photovoltaic devices, electron-hole pairs in a semiconductor material are generated by light absorption. Electron-hole pairs are separated by an electric field within a micrometer-thick depletion region, with the maximum voltage produced being equivalent to the semiconductor band gap ($\mathrm{E_g}$). In contrast, ferroelectric materials achieve charge separation through spontaneous electric polarization, resulting in a

photovoltage significantly greater than the band gap, known as the anomalous photovoltaic effect (Yang et al.). Secondly, in ferroelectric materials, the direction of photovoltage and photocurrent can be reversed by altering the polarization direction. (Choi et al., 2009). Consequently, ferroelectric materials have the potential to achieve better power conversion efficiency (PCE) compared to conventional photovoltaic materials, offering exciting possibilities for the future of solar energy and related technologies. A schematic representation of FEPV devices, including lateral and vertical structures, is shown in Figure 2.9 (Yuan et al., 2014). These devices feature two electrodes, a cathode and an anode.

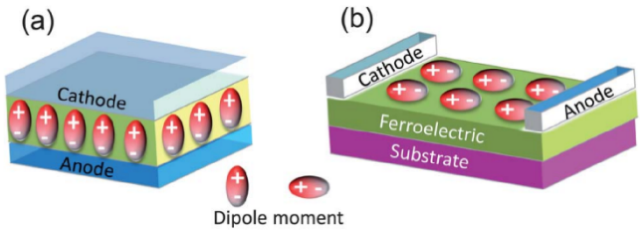

Figure 2.9 The schematic diagram illustrates the ferroelectric photovoltaic device, (a) vertical and (b) lateral configurations. (Yuan et al., 2014).

The polarization direction in ferroelectric materials is indicated by the electric dipole moment. Several factors influence the photovoltage, such as the electrodes, light intensity, remnant polarization in the ferroelectric materials, the distance between, domain walls, crystal orientation, and the interface of the ferroelectric-metal. Various mechanisms have been suggested to explain the superior voltage output of FEPV materials.

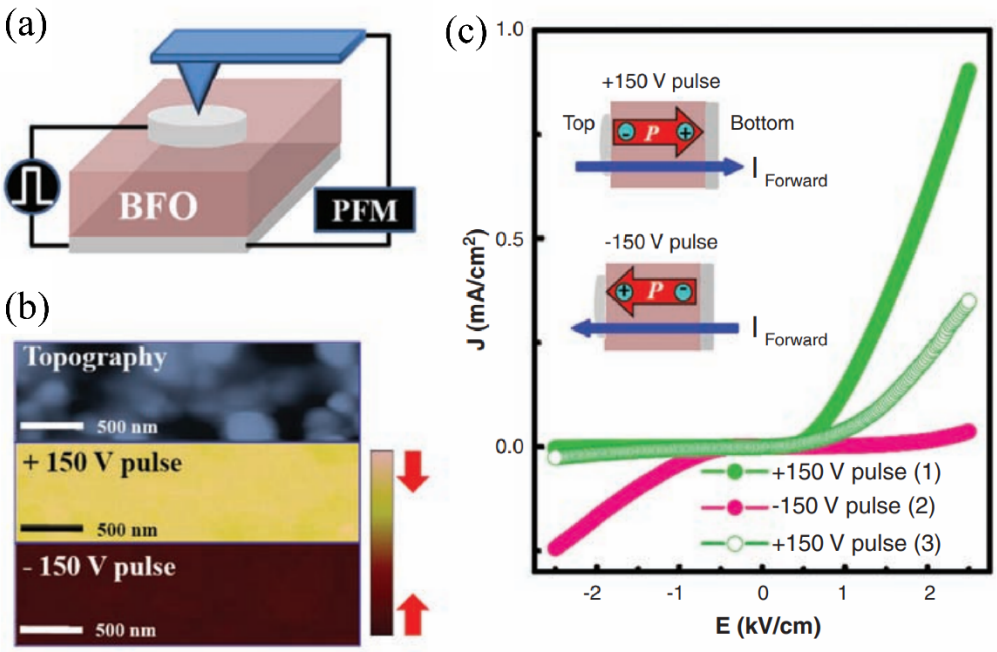

Figure 2.10 (a) The schematic setup for PFM and current density J(E) measurements on Ag/BFO/Ag samples subjected to electric pulses of ±150 V (with an electric field E≈17 kV/cm). (b) The top panel shows the topography, and the middle and bottom panels display out-of-plane PFM images color-scaled after applying +150 V and -150 V pulses, respectively. (c) The J(E) curves after applying different voltage pulses: +150 V, -150 V, and +150 V, respectively (Choi et al., 2009).

Choi et al. reported a diode effect in the BFO crystal characterized by nonlinear, unidirectional, and high electric conduction. This effect is associated with the direction of electric polarization in the bulk material. When an external electric field switches the electric polarization, the diode effect also reverses. The system consists of a thin, platelike BFO crystal with a thickness of approximately 90 μm and in-plane dimensions of about 1×2 mm², along with a circular Ag electrode of around 0.6 mm thickness, as illustrated in Figure 2.10(a). The forward and reverse bias directions are altered by applying high electric voltage pulses.

When the Ag/BFO/Ag samples are subjected to electric pulses of +150 V (with an electric field strength of approximately $\mathbf{E} \approx 17$ kV cm^{-1}) on the top electrode, the polarization direction points downward. This is evident in the Piezoresponse Force Microscopy (PFM) image displayed in Figure 2.10(b). The electric current flows downward direction through the sample, causing the diode to have a forward direction from top to bottom, as depicted in the $\mathbf{J(E)}$ curve in Figure 2.10(c) (Choi et al., 2009).

In contrast, applying -150 V electric pulses to the top electrode reversed the ferroelectric polarization orientation to the upward direction. Consequently, the diode's forward direction shifted from bottom to top, following the polarization axis, now referred to as the reverse bias direction. This is depicted by the pink line in Figure 2.10(c). After applying both +150 V and -150 V pulses, a second round of +150 V pulses was administered. However, this second application of +150 V pulses did not fully restore the original $\mathbf{J(E)}$ curve. This could be due to various factors, such as partial polarization reversal or the formation of conducting pathways (Choi et al., 2009).

2.3 Non-dynamic mechanism

2.3.1 Electronic structures of two-dimensional electron gases

A two-dimensional electron gas (2DEG) is a layer where electrons are free to move in two dimensions. At the interface of semiconductor heterostructures, such as the $LaAlO_3$ (LAO)/$SrTiO_3$ (STO) junction, a 2DEG forms due to the differing electronic properties of the materials. This confinement leads to distinctive electronic properties like high electron mobility and quantum effects (Ohtomo et al., 2004). The formation and control of a 2DEG on the bare STO surface under ultraviolet (UV) light exposure. Using angle-resolved photoemission spectroscopy (ARPES), the researchers investigate 2DEG states on lightly La-doped STO samples. The study finds that a notable 2DEG can form on the bare STO surface, akin to the one observed at the LAO/STO interface (Meevasana et al.). It shows that the 2DEG density can be controlled by adjusting the UV irradiation dose. The experiments indicate that the 2DEG on STO is likely due to oxygen vacancies created during UV exposure, rather than a polar

interface. The results offer a deeper understanding of 2DEG formation mechanisms and suggest new possibilities for oxide electronics development. The 2DEG states on the STO surface and the related momentum distribution curves are shown in Figure 2.11(a) and (b). Figure 2.11(c) displays the Fermi surface map representing the total surface charge density, consistent with 2DEG densities measured at LAO/STO interfaces (Kalabukhov et al., 2007). Figure 2.11(d) depicts the schematic Fermi surface and band dispersions derived from the measured electronic structure. These results demonstrate that a 2DEG can be generated on the UV-irradiated STO surface (Meevasana et al., 2011).

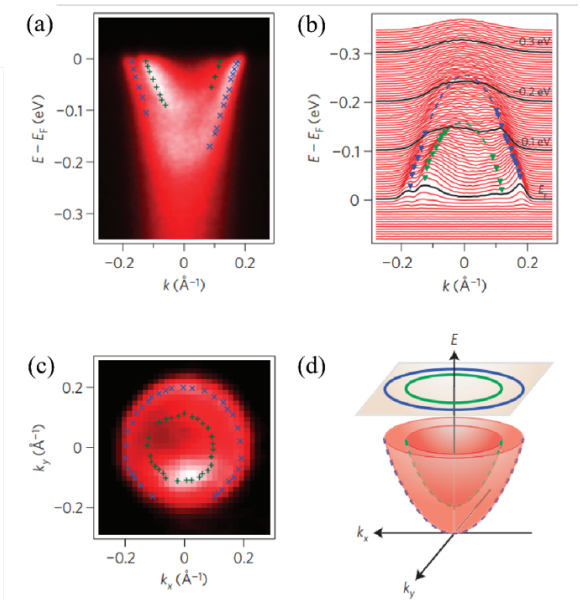

Figure 2.11 The 2DEG states of La-doped STO after UV light exposure. (a) ARPES data of La-doped STO at T = 20 K, (b) Corresponding momentum distribution curves with parabolic fits to the data points. (c) Fermi surface map. (d) Schematic Fermi surface and band dispersions obtained from the electronic structure measurement. (Meevasana et al., 2011).

Recently, the 2DEG has been studied in perovskite heterostructures, specifically at the BFO and STO interfaces. Theoretical calculations indicate that the 2DEG forms at the $(BiO)^{+}$ and $(TiO_2)^{0}$ interfaces (Zhang et al., 2011). From a chemical standpoint, the BFO/STO heterostructure exhibits similar characteristics to the

LAO/STO heterostructure. However, BFO demonstrated both ferroelectric and magnetic characteristics at room temperature (Catalan et al., 2009; Ederer et al., 2005; Lebeugle et al., 2007), a distinction that LAO lacks. The BFO/STO structure is distinct from the LAO/STO structure in its formation of a metallic character due to a 2DEG state. Conductive atomic force microscopy (C-AFM) was used to examine a 20 μm-thick cross-sectional sample of the BFO/STO interface. Figure 2.12 shows the surface topographic imaging and nanoscale current mapping of this interface. The results indicated a significantly higher current at the interface compared to the bulk materials, suggesting the formation of a 2DEG due to its conductive nature. According to (Chen et al., 2015), this phenomenon is attributed to the variation in valence state caused by the diffusion of Ti from STO into the Fe sites of BFO at the interface.

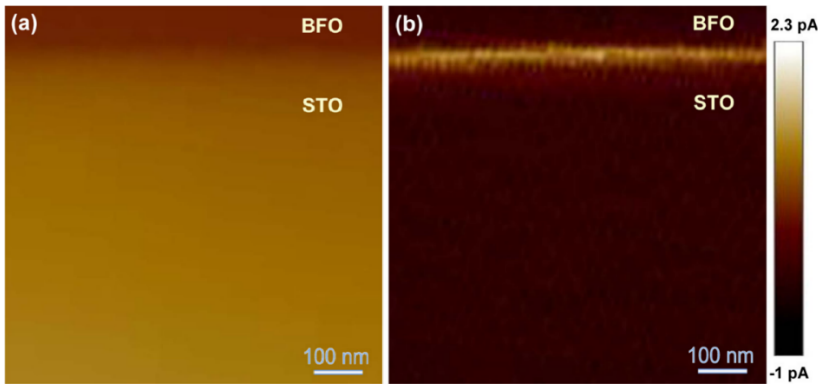

Figure 2.12 The presence of a 2DEG at the interface between BFO and STO is demonstrated using (a) a surface topography image and (b) nanoscale current tracing (Chen et al., 2015).

The conducting interface can be controlled by the ferroelectric polarization of a BFO/STO superlattice (Fu et al., 2021) and a BFO/$TbScO_3$ (TSO) heterostructure (Zhang et al., 2018) Under UV irradiation, the formation of a 2DEG state induced by oxygen vacancies has been reported in the slightly doped metal $Bi_{0.95}La_{0.05}FeO_3$ (BLFO) (Nathabumroong et al., 2020). So far, creating a 2DEG has required epitaxially grown BFO thin films. To achieve this, BFO thin films need to be grown on STO (100) substrates at high temperatures (580-750 °C) (Ji et al., 2010; Nakashima et al., 2015; Nakashima et al., 2020; Saenrang et al., 2017). However, there

are a few studies on amorphous oxides on STO substrates that can also create a 2DEG through the formation of oxygen vacancies (Lee et al., 2012; Li et al., 2018; Scigaj et al., 2015).

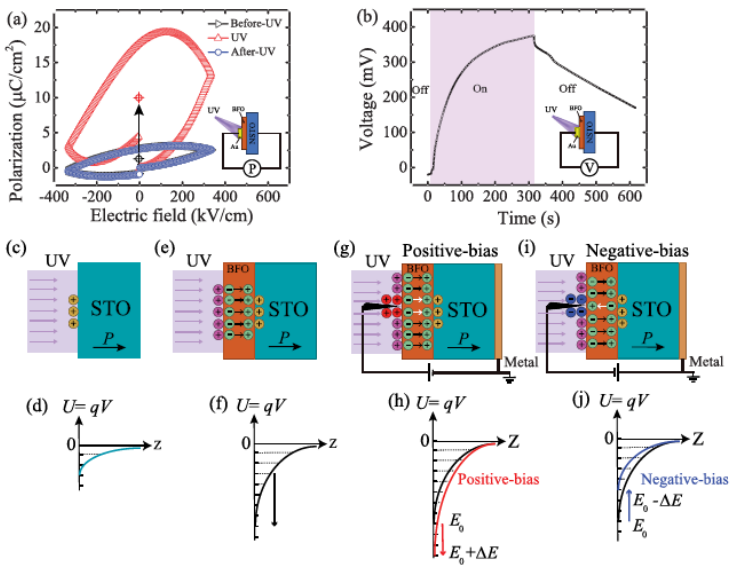

Figure 2.13 Mechanisms of 2DEG formation and modulation in amorphous BFO/NSTO thin films Interface (a) the polarization-electric field (P-E) hysteresis loops of under UV illumination. This indicates the electrical polarization behavior which contributes to the formation of the 2DEG. (b) Illustrates the time-dependent voltage with UV irradiation cycles. This voltage difference is related to the induced electric field and polarization, crucial for understanding the modulation of 2DEG. (c)–(j): Provide schematic diagrams of UV-light-induced oxygen vacancies and the resultant quantum well states (Laohana et al., 2022).

In 2022, Peerawat Laohana and co-workers studied the photo-induced conductivity of a 2DEG at the interface of STO and BFO. The BFO is deposited using radio frequency magnetron sputtering. The findings show a significant increase in photo-induced conductance at the BFO/STO interface, up to 20.62 times higher than the sum of individual BFO and STO conductance. This enhancement is attributed to the strong photo-induced electrical polarization of BFO, which can be modulated by an electric field, exhibiting diode-like behavior. In figure 2.13 demonstrates the mechanisms behind the formation and modulation of a 2DEG at the BFO/STO interface.

UV light induces oxygen vacancies in the STO, forming a quantum well that traps electrons to create the 2DEG. The polarization of the BFO layer, enhanced by UV illumination, further deepens this quantum well, increasing the carrier density and conductivity. Applying an external electric field can modulate these effects, allowing for control over the 2DEG properties, which is crucial for potential optoelectronic applications (Laohana et al., 2022).

2.3.2 Effects of oxygen vacancy

Oxygen vacancies are the most common defect in certain metal oxides and play a crucial role in electrical conductivity (Tanaka et al., 2002). In metal oxides, light exposure can create oxygen vacancy states between the valence and conduction bands. Research by Suwanwong et al. showed that 2DEG states form on the UV-irradiated surface of single crystal STO (100). UV light causes oxygen vacancies in STO, changing its resistance (Suwanwong et al., 2015). These 2DEG states contribute significantly to surface conductivity. To measure resistivity, a setup with gold electrodes in an interdigitated pattern was used, as shown in Figure 2.14(a). Before UV exposure, the resistance of the STO sample at 2×10^{-8} mbar was around 4 GΩ. Under UV light, the creation of 2DEG reduced the resistance to below 10 MΩ. When the UV light was turned off, the resistance gradually returned to its initial state, although more slowly, due to the persistent 2DEG. This behavior over time is similar to the ARPES data shown in Figure 2.11. Additionally, Jaiban et al. conducted a measurement of conductance on STO under UV light with a wavelength of 405 nm. The light was applied between two gold electrodes that were positioned 2 mm apart, as shown in Figure 2.14(b).

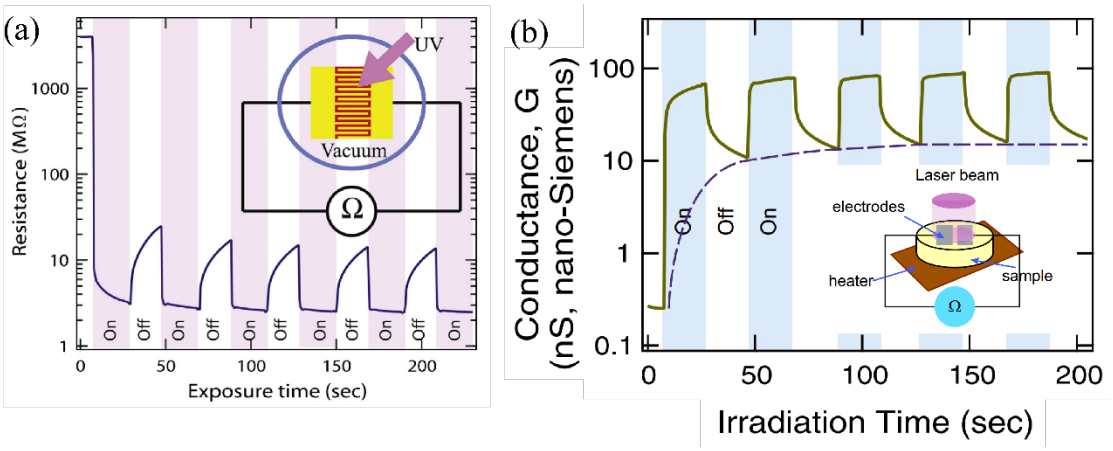

Figure 2.14 The resistance of the STO surface was measured during the on-off UV irradiation. The measurement setup diagram is shown in the inset figure. Study by (a) Suwanwong et al. (Suwanwong et al., 2015) and (b) Jaiban et al. (Jaiban et al., 2020), provide the details of these measurements and setups, respectively.

The conductance in the off state, influenced by the slow changing 2DEG, increased with longer exposure times, matching the increase in surface carrier densities seen in ARPES data (Jaiban et al., 2020). These findings highlight the significant impact of 2DEG on resistance and conductance changes. In 2024, Siwat Polin conducted a study to examine the magneto-optical Kerr effect (MOKE) in monodomain BFO thin films. The research focused on the impact of applied electric fields and light irradiation. The results show that the Kerr rotation of BFO changes under these conditions, indicating the ability to control the Kerr rotation using both electric fields and light irradiation.

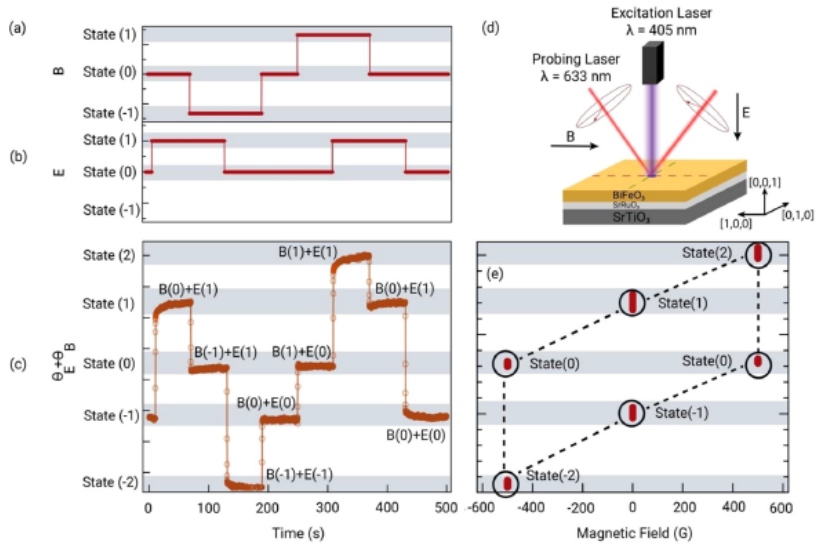

Figure 2.15 Coupling Mechanism between magnetic field and electric field or UV light via Kerr angle measurements in BFO films. (a) an applied magnetic field in units of Gauss and (b) an electric field or UV-light irradiation in units of W/m^2. (c) Changes in the Kerr angle ($\theta_B + \theta_E$) obtained from the applied magnetic field and electric field or UV-light irradiation. (d) A schematic illustrating the interaction between the magnetic field and the electric field or UV light through the Kerr-rotation measurement of the BFO film. (e) Changes in the states of BFO when an electric field, UV light, and a magnetic field are added or removed, measured in units of the Kerr angle. (Polin et al., 2024).

The Kerr angle in BFO thin films is influenced by the creation of oxygen vacancies, which enhance electrical polarization and modify magnetic properties. UV irradiation generates these vacancies, leading to a photo-voltage effect that increases polarization. This increased polarization interacts with the magnetic field, changing the Kerr angle. Figure 2.15 highlights the potential for using BFO in multifunctional devices that leverage the coupling between electric, magnetic, and optical properties (Polin et al., 2024).